



Evolution of solidification microstructure and dynamic recrystallisation of Inconel 625 during laser solid forming process

Y. L. Hu^{1,2}, X. Lin^{1,2,*}, X. F. Lu^{1,2}, S. Y. Zhang^{1,2}, H. O. Yang^{1,2}, L. Wei^{1,2}, and W. D. Huang^{1,2,*}

¹ State Key Laboratory of Solidification Processing, Northwestern Polytechnical University, 127 Youyixilu, Xi'an 710072, Shaanxi, People's Republic of China

² Key Laboratory of Metal High Performance Additive Manufacturing and Innovative Design, MIIT China, Northwestern Polytechnical University, 127 Youyixilu, Xi'an 710072, Shaanxi, People's Republic of China

Received: 24 May 2018

Accepted: 11 July 2018

Published online:

26 July 2018

© Springer Science+Business Media, LLC, part of Springer Nature 2018

ABSTRACT

This study investigated the evolution of solidification microstructure and dynamic recrystallisation (DRX) during the laser solid forming of the Ni-based Inconel 625 superalloy. The as-deposited microstructure mainly showed epitaxially grown columnar grains with fine equiaxed grains between them. These fine equiaxed grains were formed by the discontinuous DRX (DDRX) and continuous DRX (CDRX) processes, which were induced by the cyclic thermal stress resulting from the repeated laser deposition. The bulging of pre-existing grains and sub-grain rotation were the main mechanisms of the DDRX and CDRX phenomena, respectively. Additionally, after the occurrence of DRX, the dislocations were released and there was no distortion in the recrystallised grains. Coarse equiaxed grains were present in the top zone of the deposit; these grains were formed by the columnar-to-equiaxed transition during the solidification of the molten pool after the end of the laser re-melting and deposition process.

Introduction

Inconel 625 is a kind of solid-solution-strengthened Ni-based superalloy, which has excellent corrosion resistance and mechanical properties at high temperature. Owing to its simultaneously high processability and weldability, this superalloy is widely used for various advanced industrial applications, e.g. in aerospace engines, chemical equipment, and nuclear

industries [1–5]. Recently, with the development of additive manufacturing (AM), laser solid forming (LSF) has emerged as an advanced high-performance AM technology that is capable of solid free-form fabrication of complex Ni-based superalloy components in the energy and power fields, while also providing considerable cost savings and enabling high material utilisation. Thus far, laser-solid-formed

Address correspondence to E-mail: xlin@nwpu.edu.cn; huang@nwpu.edu.cn

(LSFed) Ni-based components have been successfully used in industries such as the aerospace industry [6].

However, because of the high thermal expansion coefficient of the Inconel 625 superalloy and the repeated rapid local heating and cooling occurring during the LSF process, extremely high thermal stress is typically generated in LSFed Inconel 625. This means that the excessive thermal stress may cause plastic deformation of the deposited layers. Wang et al. [7] used the finite-element method (FEM) to calculate the residual stress distribution in a single wall of the Inconel 625 superalloy fabricated by LSF and validated the predictions of the thermomechanical model via neutron diffraction measurements. They found that the maximum residual stress in the deposit was 600 MPa, and the residual stress first increased and then decreased in the length direction from the substrate to the top of the centre plane of the deposit. In addition, compressive stresses were observed in most regions, whereas tensile stresses were observed at the top of the wall.

Under the influence of thermal stress, the deposit geometry will deviate from the designed dimensions of components during the LSF process. Additionally, thermal and residual stresses will also promote the formation of microcracks and reduce the tensile strength and fatigue performance [8–11]. In recent years, numerous studies have been conducted for reducing the thermal and residual stresses during the AM process [12–14]. However, with the deposition of the succeeding layers, the already deposited layers will be subjected to high-temperature annealing or tempering treatment repeatedly, with the maximum temperature being close to the melting point; as a result, these thermal and residual stresses can also induce a complex solid-state phase transformation in the deposit, such as dynamic recrystallisation (DRX) and precipitation of the second phase. In addition, face-centred-cubic (FCC) metals are prone to DRX during hot deformation, because they have low stacking fault energies (SFEs) [15, 16]. Because the Ni-based Inconel 625 superalloy has an FCC matrix, DRX may occur in an Inconel 625 deposit under the influence of thermal and residual stresses during the LSF process. Dinda et al. [17] investigated the microstructural evolution and thermal stability of the Inconel 625 superalloy fabricated by LSF, and they found that the columnar dendrites in the Inconel 625 superalloy deposit remained stable up to 1000 °C ($\sim 3/4 T_m$) and a fully recrystallised equiaxed

structure was visible at around 1200 °C. They thought that the driving force for the recrystallisation was residual stress, but they did not provide much evidence or a reasonable explanation for this belief. Liu et al. [18] found that Inconel 718 fabricated by LSF was recrystallised after solution treatment at 1100 °C, and they confirmed that the residual stress in the deposit promoted static recrystallisation in the as-deposited columnar grains during the solution heat-treatment process.

If DRX is induced in the LSF process, it can use up the pre-generated residual stress and refine the initial coarse columnar grains in the already deposited layers. Thus, the modified stress state and microstructure following DRX will consequently improve the mechanical properties of the material. However, very few studies have attempted to investigate the DRX phenomenon in Ni-based superalloys during the LSF process. Furthermore, the conditions and mechanisms of DRX in these superalloys remain unclear. In the present study, therefore, the microstructural evolution of the Inconel 625 superalloy during the LSF process was studied, and the columnar-to-equiaxed transition (CET) and DRX occurring in the deposit were mainly discussed.

Materials and experimental procedure

Materials and laser processing parameters

The particle size of Inconel 625 superalloy powders was 50–150 μm ; the chemical composition of the powders is listed in Table 1. Before the LSF process, the substrate was polished with sandpaper and cleaned with acetone, and the powders were dried under vacuum for 3 h at 120 °C. The substrate was a forged Inconel 625 superalloy plate having dimensions of 100 mm \times 80 mm \times 10 mm, and the size of the deposited sample was 80 mm \times 15 mm \times 10 mm (25 layers). The laser used was a continuous-wave semiconductor laser with a maximum output

Table 1 The chemical compositions of the Inconel 625 alloys (wt.%)

| Ni | Cr | Mo | Nb | Fe | Ti | Al | Si | C |
|------|----|-----|-----|----|-----|-----|-----|------|
| Bal. | 22 | 8.5 | 3.6 | 2 | 0.2 | 0.2 | 0.5 | 0.01 |

power of 6 kW and a wavelength of 1.06 μm . The laser processing parameters are listed in Table 2.

Microstructural characterisation

A Keyence VHX-2000 optical microscope (OM) and a TESCAN VEGA II-LMH scanning electron microscope (SEM) equipped with an electron backscatter diffraction (EBSD) unit were used for characterising the microstructural evolution. The deposited sample was ground on 80–2000-grit silicon carbide paper and then polished using colloidal silica (0.05 μm grit size) in a vibratory finishing machine. To reveal the macrostructure and microstructure of the LSFed Inconel 625 superalloy, the sample was electrolytically etched under a 10-V direct current for 15 s in a reagent of 10% aqueous chromic acid solution. The evolutions of the texture and orientation were characterised by EBSD. The distributions of different elements were measured using a Shimadzu 1720 electron probe micro-analyser (EPMA). A Tecnai G2F30 transmission electron microscope (TEM) was used to examine the dislocations in the deposit.

Thermomechanical simulations

The evolution and distribution of the temperature field during LSF of the Inconel 625 superalloy were simulated by the FEM. During the simulation process, the birth-dead-elements technique is used [19]. Before the deposition process, all the elements of deposit are inactive. According to the deposition sequence, at each time step the elements are activated by an octree-based searching algorithm.

Table 2 The processing parameters of the LSF experiment

| Parameter | value |
|-----------------------------|-------|
| Laser power (W) | 1500 |
| Scanning velocity (mm/min) | 900 |
| Spot diameter (mm) | 2 |
| Powder feeding rate (g/min) | 7.5 |
| Increment of Z (mm) | 0.4 |
| Overlap (%) | 50 |

Transient thermal model

In LSF, the governing equation for transient heat conduction for a component subjected to a volumetric heat source is given as:

$$Q(x, t) - \nabla \cdot q(x, t) = \rho C_p \frac{dT}{dt} \quad (1)$$

where ρ is the density of the Inconel 625 superalloy, taken as $8.1 \text{ g} \cdot \text{cm}^{-3}$; C_p is the temperature-dependent specific heat capacity; T is the temperature; t is the time; Q is the time- and location-dependent volumetric heat source; and q is the conductive heat flux through the material. Three kinds of heat transfers are considered to occur in the LSF process: conductive heat transfer (q), radiative heat transfer (q_{rad}), and convective heat transfer (q_{conv}). These three heat transfer processes follow the Fourier law, the Stefan–Boltzmann law, and Newton’s convective cooling law, respectively:

$$q = -k \nabla T \quad (2)$$

$$q_{\text{rad}} = \varepsilon \sigma_b (T_S^4 - T_\infty^4) \quad (3)$$

$$q_{\text{conv}} = h(T_S - T_\infty) \quad (4)$$

where k is the temperature-dependent thermal conductivity; ε is the surface emissivity; σ_b is the Stefan–Boltzmann constant; T_S and T_∞ are the surface temperature of the deposit and ambient temperature, respectively; and h is the convective heat transfer coefficient.

Mechanical model

The governing mechanical stress equilibrium equation is expressed as:

$$\nabla \cdot \sigma = 0 \quad (5)$$

where σ is the third-order stress tensor.

The mechanical constitutive law can be expressed as:

$$\sigma = C \varepsilon_e \quad (6)$$

where C is the fourth order stiffness tensor, and the elastic strain, ε_e is computed as:

$$\varepsilon_e = \varepsilon - \varepsilon_p - \varepsilon_T \quad (7)$$

where ε is the total strain, ε_p is the plastic strain and ε_T is the thermal strain.

Heat source model and boundary conditions

The average volumetric heat source model for laser beam is expressed as:

$$Q_{(x,t)} = \frac{\eta P}{V} \tag{8}$$

where η is the laser absorption of alloy, P is the laser power, and V is the volume affected by the heat source.

The temperature-dependent thermalphysical properties of the Inconel 625 superalloy are listed in Table 3. The emissivity ϵ of Inconel 625 is taken as 0.28 as found in Ref. [21]. The convective heat transfer coefficient h is 18 W/m²/ °C.

Figure 1 shows the schematic of the finite-element mesh of the additively manufactured Inconel 625 deposit. In the central portion of the deposit, six points are selected along the deposition direction to analyse the temperature field during the LSF process. Point A represents the point of contact with the substrate, and points B–F correspond to positions at distances of 0.8, 1.6, 3.2, 6.4, and 10 mm, respectively, from the substrate; points B–F also correspond to the positions of the 2nd layer, 4th layer, 8th layer, 16th layer, and 25th layer, respectively.

Results and discussion

Evolution of solidification microstructure

Figure 2a shows the macrostructure in the vertical plane of the LSFed Inconel 625 superalloy, and Fig. 2b–d shows the detailed OM microstructures in different zones-top, middle, and bottom zones, respectively, along the deposition direction. Figure 3 shows EBSD maps of the substrate and as-deposited Inconel 625 superalloy. From Fig. 2b, it is found that

the bottom of the deposit contains typical epitaxially grown columnar grains, and the width of the columnar grains near the substrate is only 20 μm, which is approximately equal to the grain size of the forged substrate. However, as the deposit height increases, the width of the columnar grains also increases until it exceeds 200 μm, after which it remains stable with a further increase in the deposit height. Additionally, some fine equiaxed grains are present in between the columnar grains in the middle zone of the deposit, as shown in Fig. 3c. The size of the columnar grains in this zone is larger than that in the bottom zone, and the growth of the columnar grains between the layers occurs in a zigzag direction. Furthermore, the finer the equiaxed grains formed at the columnar-grain boundaries and even inside the columnar grains, the more detailed is the microstructure, as depicted in Fig. 3c. The microstructure of the top zone in the deposit is shown in Figs. 2d and 3d; obvious equiaxed grains are visible in the top zone, and these equiaxed grains are larger than 200 μm in size; this size is larger than that of equiaxed grains observed in the bottom and middle zones.

The microstructure and detailed Laves phase distribution in the different zones in the deposit are shown in Fig. 4. It can be seen that the average primary dendrite arm spacing ($\bar{\lambda}_1$) gradually increases from the bottom zone ($\bar{\lambda}_1 = 5 \mu\text{m}$) to the top zone ($\bar{\lambda}_1 = 10 \mu\text{m}$) in the deposit. Meanwhile, the secondary dendrite arm gradually becomes more apparent, as shown in Fig. 4a, c, e. The reason for this phenomenon is that with an increase in the deposit height, the deposited part is subjected to subsequent thermal cycling, which results in an increase in the temperature of the deposited layers. Thus, the temperature gradient (G) of the molten pool in the

Table 3 Temperature-dependent thermal properties of Inconel 625 where T is the temperature, k is the thermal conductivity, C_p is the specific heat, E is the Young modulus, σ_y is the yield strength, and α is the coefficient of expansion. [20]

| T (°C) | k (W/m/ °C) | C_p (J/kg) | E (GPa) | σ_y (MPa) | α (μm/m °C) |
|----------|---------------|--------------|-----------|------------------|--------------------|
| 20 | 9.9 | 410 | 208 | 493 | 12.8 |
| 93 | 10.8 | 427 | 204 | 479 | 12.8 |
| 205 | 12.5 | 456 | 198 | 443 | 13.1 |
| 315 | 14.1 | 481 | 192 | 430 | 13.3 |
| 425 | 15.7 | 511 | 186 | 424 | 13.7 |
| 540 | 17.5 | 536 | 179 | 423 | 14.0 |
| 650 | 19.0 | 565 | 170 | 422 | 14.8 |
| 760 | 20.8 | 590 | 161 | 415 | 15.3 |
| 870 | 22.8 | 620 | 148 | 386 | 15.8 |

Figure 1 Schematic of finite-element mesh of Inconel 625 additively manufactured deposition, where point A represents the point of contact with the substrate, B, C, D, E, F indicate the position with the distance from the substrate of 0.8, 1.6, 3.2, 6.4 and 10 mm, respectively.

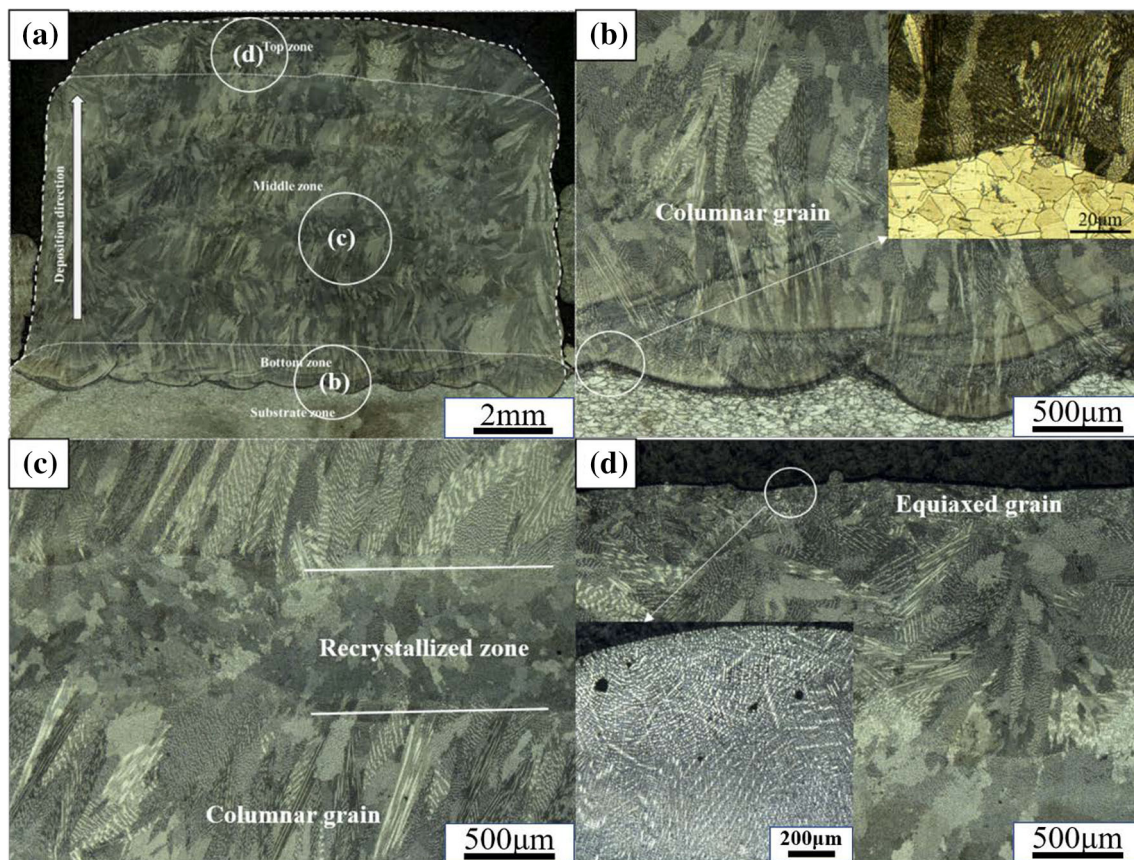
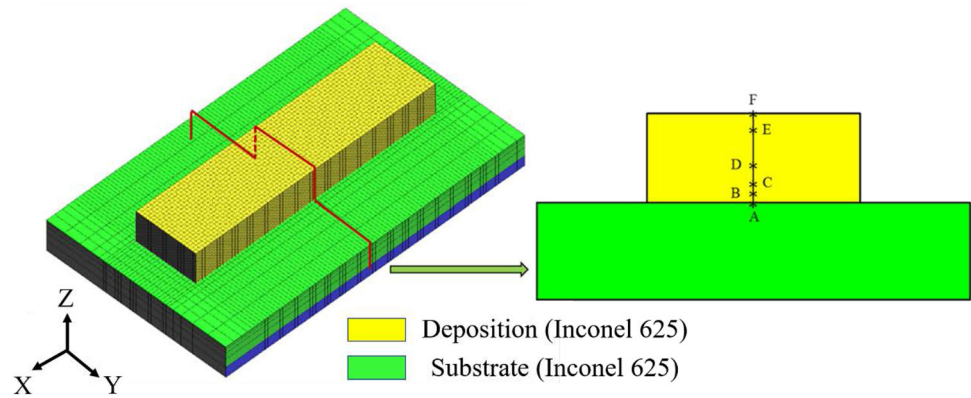


Figure 2 Macrostructure of Inconel 625 fabricated by LSF (b) bottom zone; (c) middle zone; (d) top zone.

subsequent layers decreases. The dendritic growth theory indicates that the average primary dendritic spacing ($\bar{\lambda}_1$) has an approximate relationship with the solidification velocity (V) and the temperature gradient (G) [22]:

$$\bar{\lambda}_1 \propto V^{-a} G^{-b} \quad (5)$$

Here, a and b are constants associated with alloys.

In addition, the size of bright second phases in interdendritic regions increases with the deposit height. The formation of a Laves phase in Nb-bearing superalloys is caused by the significant segregation of Nb in the interdendritic regions [23, 24]; this segregation promotes the formation of the secondary phases observed in the microstructure of LSFed Inconel 625. The distribution of the Nb element in different zones is shown in Fig. 5. It can be seen that

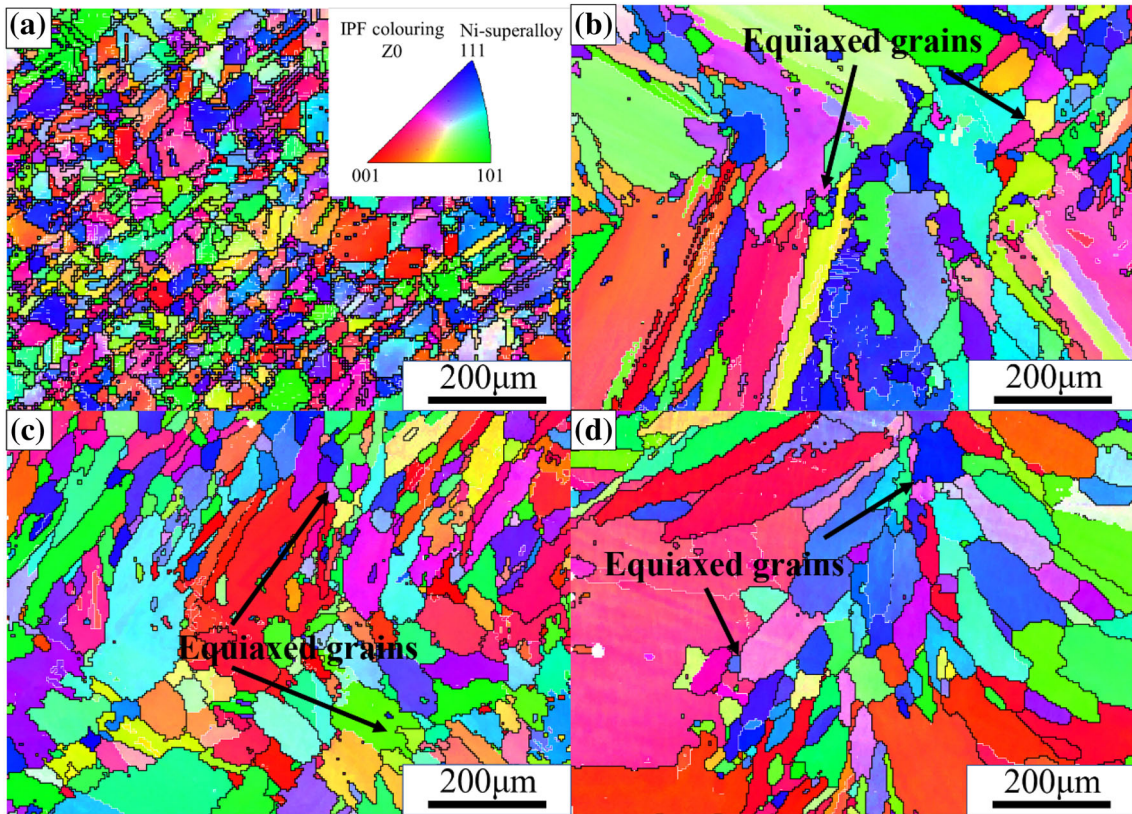


Figure 3 EBSD maps of the as-deposited Inconel 625 superalloy. **a** Inverse pole figure (IPF) coloured OIM map of substrate, **b** OIM of bottom zone, **c** OIM of middle zone, **d** OIM of top zone.

maximum microsegregation of Nb occurs in the bottom region of the deposit, whereas microsegregation occurs to a lesser extent in the top region. The elemental distribution coefficient k represents the intensity and direction of microsegregation of an element in the solidification process. The solidification velocity dependence of k_V for dilute solutions can be expressed as

$$k_V = \frac{k_e + (a_0V/D)}{1 + (a_0V/D)} \tag{6}$$

where k_e is the equilibrium partition coefficient, D is the solute diffusion coefficient at the solid–liquid interface, V is the solidification velocity, and a_0 is a length of atomic dimensions. k_e , D , and a_0 for Nb in Inconel 625 are constants; therefore, k depends only on the solidification velocity (V). It can be deduced that the solidification velocity increases with increasing deposition height; as a result, the solute partition coefficient in the bottom zone is smaller than that in the top zone of the deposit, and maximum microsegregation of Nb occurs in the bottom zone. However, the temperature gradient (G) of the

top zone is smaller, and the cooling rate (ε) decreases as the deposit height increases; therefore, the average primary dendrite arm spacing ($\bar{\lambda}_1$) in the top zone of the deposit is larger than those in the other regions and the secondary dendrite arm gradually becomes more apparent. Although the microsegregation of Nb in the top zone is weaker, the Laves phase has a longer growth time and a larger growth space than those in the bottom zone. As a result, the Laves phase becomes larger with increasing height of the deposit.

Columnar-to-equiaxed transition

Figure 6 shows the simulated temperature field change during the LSF process. It can be seen that the temperatures of most of the 25 deposited layers are mainly in the range of 800–1050 °C during LSF, owing to the repeated thermal cycling and heat accumulation. Additionally, with an increase in the deposit height, the temperature of the deposited layers also increases noticeably. Manvatkar et al. [25] investigated the heat transfer and material flow during the LSF process, and they found that the

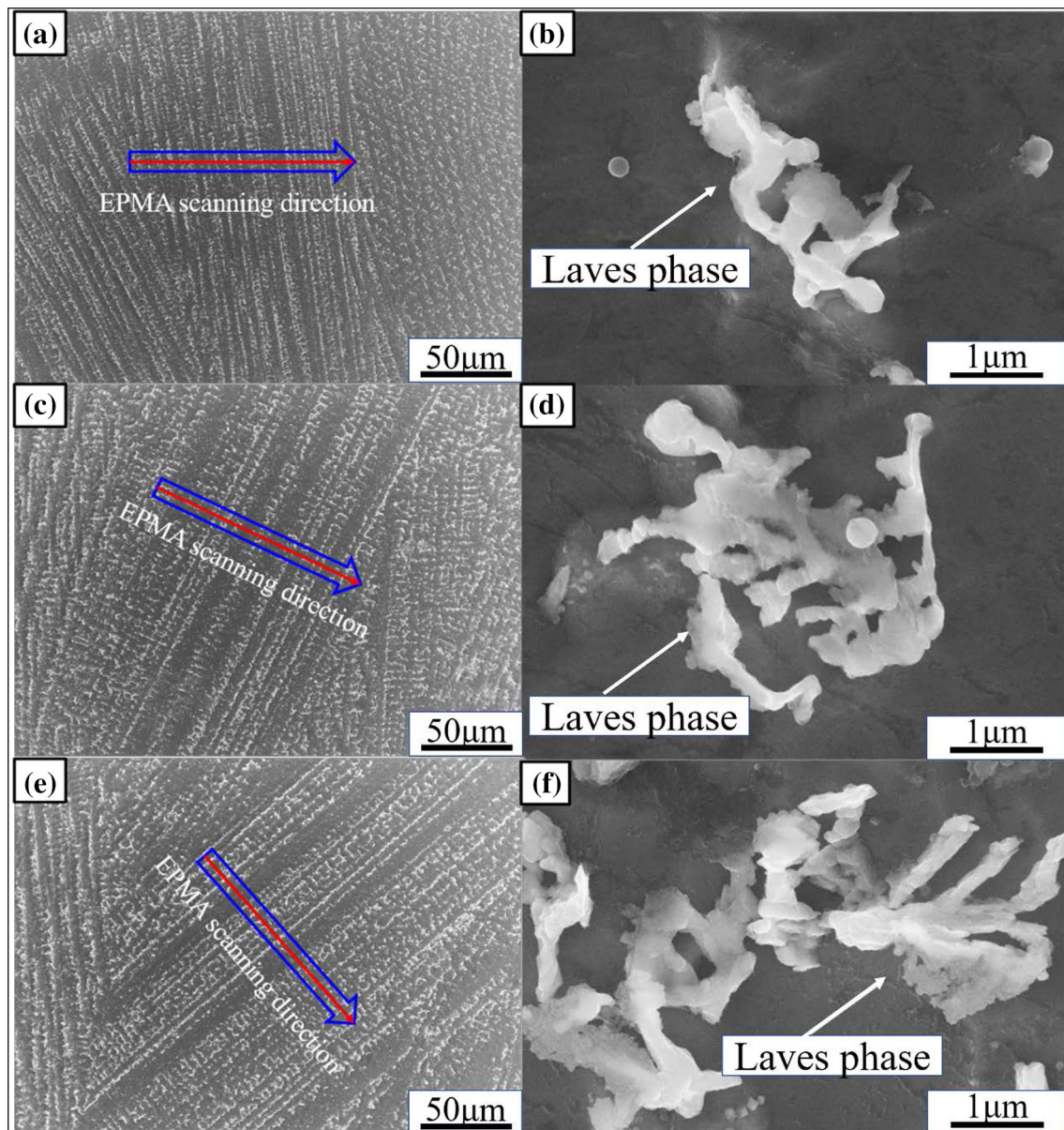


Figure 4 Microstructure and Laves phase in different zones of deposited Inconel 625. **a, b** Bottom zone; **c, d** middle zone; **e, f** top zone.

temperature field of the deposit in the LSF process is affected mainly by the power density of the heat source, the absorption rate of alloy powders, and the heat dissipation conditions. High power density and high absorption rate of the material can lead to a wide distribution of the temperature field in the deposit. Furthermore, the power density of the laser is controlled mainly by the laser power, laser wavelength, and spot diameter. In this study, because the power of the semiconductor laser is 1500 W and the laser wavelength is 1.06 μm , the absorption rate of the Ni-based superalloy is 0.35 [26]. In addition, the

geometric size of the deposit is larger and the heat dissipation is weaker than that in single-wall samples. As a result, the temperature inside the LSFed sample remains higher for a long time.

During the LSF process, metal powder is injected into a molten pool formed by controlled laser heating, as shown in Fig. 7. Hu et al. [27] investigated the thermal behaviour of the molten pool during the LSF process and found that the geometry of the molten pool, the temperature distribution inside it, and the solidification conditions during the LSF process were affected mainly by the power of the laser (P), the

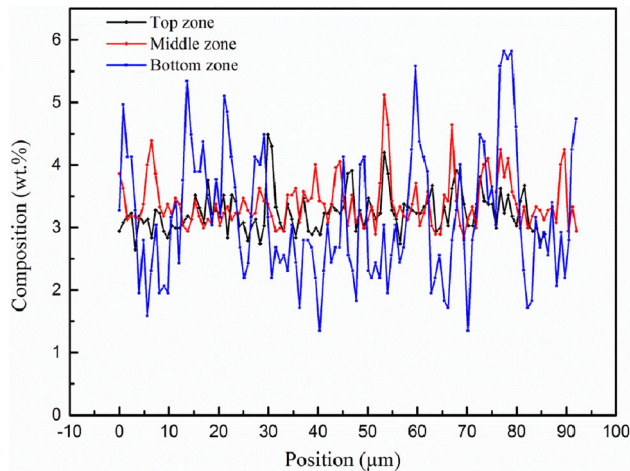


Figure 5 Distribution of Nb element measured by EPMA in different zones. Blue, red, and black lines refer to bottom, middle, and top zones of the deposit, respectively.

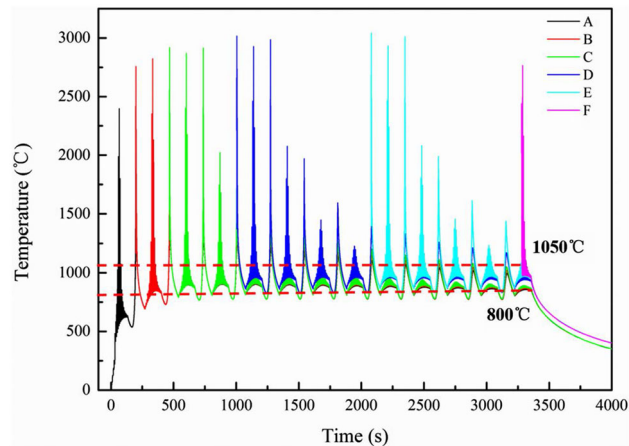


Figure 6 The temperature of the length direction in the centre plane of the built as a function of time simulated by FEM.

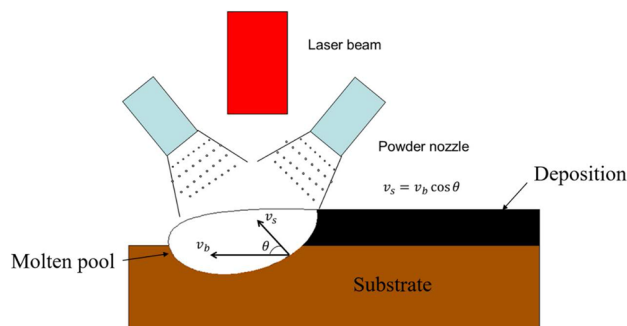


Figure 7 Schematic of laser solid forming processing.

beam velocity (V_b), and the beam diameter (D). Figure 8 shows the morphology and temperature distribution of the molten pool in different layers. It can

be seen that with an increase in the deposition height, the molten pool becomes increasingly larger. From the temperature distribution and geometry of the molten pool, the temperature gradient G and solidification velocity V can be obtained. Figure 9 shows the evolution of the local solidification conditions of the first layer along the solidus isotherm; it can be seen that the temperature gradient G decreases from the bottom of the molten pool to the top, whereas the solidification velocity V increases in the same manner. In this study, the LSF parameters are constant, but the temperatures of the different layers are different. The size and geometry of the molten pool in the different layers are controlled mainly by the temperatures of the deposited layers.

The top zone of the deposit is the last solidified zone, and it can be seen in Fig. 2d that the CET occurs in the top zone. The CET phenomenon is a common occurrence in the LSF process. Several models have been proposed previously for explaining this phenomenon [28–31]. Under the condition of directional solidification, an element ($k < 1$) will be enriched in the front of the solidification interface to form the constitutional supercooling zone. When the maximum local undercooling is higher than the nucleation undercooling, formation of equiaxed dendrites is possible. However, if the volume fraction of the equiaxed dendrites is too small, they will be wrapped into the columnar dendrites. The CET occurs when the volume fraction of equiaxed dendrites reaches a certain value to block the growth of the columnar dendrites. According to the CET model developed by Lin et al. [32], the growth of columnar and equiaxed dendrites can be described as

$$\sum_{i=1}^{n-1} m_{vi} G_{Ci} \xi_C(Pe_i) - G = \frac{\Gamma}{\sigma^* r^2} \tag{7}$$

where

$$m_{vi} = m_i \left\{ 1 + \frac{k_i - k_{vi} [1 - \ln(k_{vi}/k_i)]}{1 - k_i} \right\} \tag{8}$$

$$k_{vi} = \frac{k_i + a_0 v / D_i}{1 + a_0 v / D_i} \tag{9}$$

$$G_{Ci} = - \frac{(1 - k_{vi}) v C_i^*}{D_i} \tag{10}$$

$$\xi_C(Pe_i) = 1 - \frac{2k_{vi}}{[1 + (1/\sigma^* Pe_i^2)]^{1/2} - 1 + 2k_{vi}} \tag{11}$$

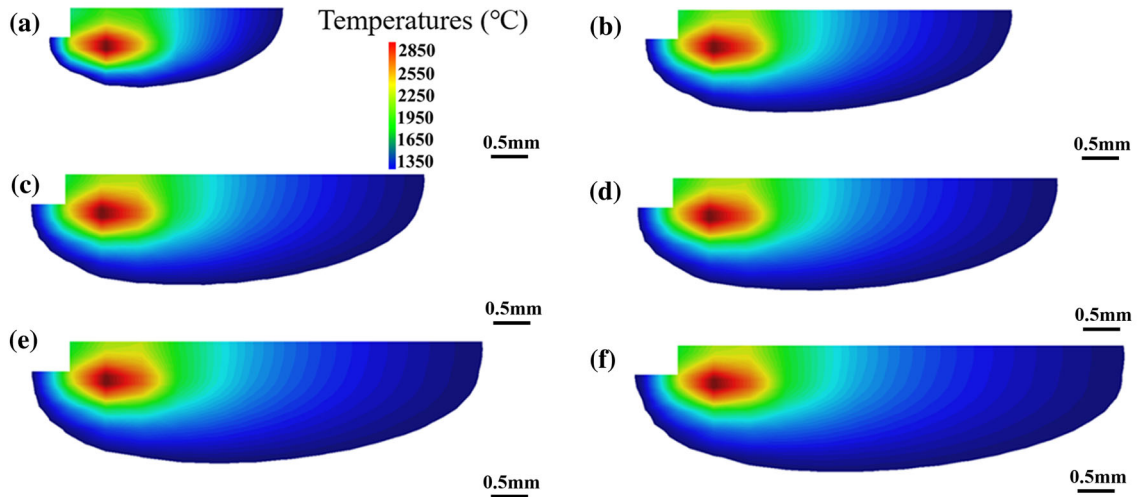


Figure 8 The molten pool morphology and temperature field of different layers. **a** 1st layer, **b** 2nd layer, **c** 4th layer, **d** 8th layer, **e** 16th layer, and **f** 25th layer.

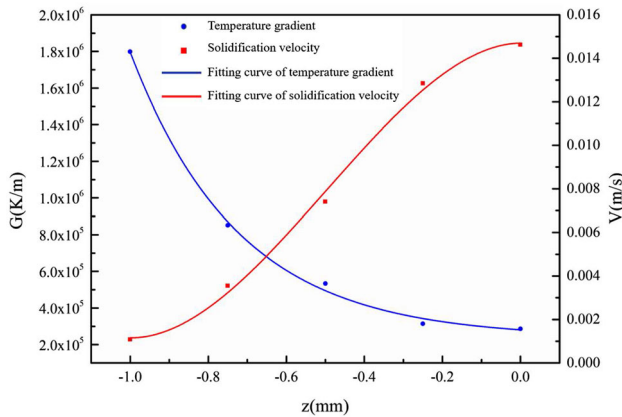


Figure 9 Evolution of the local solidification variables G and V as the depth z ($z = 0$ corresponding to the surface) for 1st layer.

The control parameters for columnar dendritic growth are the solidification velocity (V) and temperature gradient (G), whereas that for equiaxed dendritic growth is the melt undercooling. The distribution of the subcooling zone in the deposit can be obtained by solving the dendrite tip radius r and dendrite tip temperature $T_{c/d}$ in front of the growth interface of columnar dendrites.

$$T_{c/d} = T_m + \sum_{i=1}^{n-1} m_{vi} C_i^* - \frac{2\Gamma}{R} - \frac{R_g T_m}{v_0 \Delta S_f} v - \frac{G\bar{D}}{v} \quad (12)$$

$$T_m = T_L - \sum_{i=1}^{n-1} m_i C_{0i} \quad (13)$$

$$C_i^* = C_{0i} / [1 - (1 - k_{vi}) I v (Pe_i)] \quad (14)$$

The maximum radius of the equiaxed dendritic growth can be obtained from the following integral:

$$r_e = \int_0^{Z_n} \frac{v_e[z]}{v} dz \quad (15)$$

Here, $v_e[z]$ is the growth velocity of equiaxed dendrites at the location distance z from the columnar dendritic tip, which can be obtained by the equiaxed dendritic growth model from the local concentration and undercooling. Z_n is the distance from the columnar dendrite tip to the point where the undercooling in the liquid is equal to the nucleation undercooling (ΔT_n). Owing to the randomness of the nucleation, the volume fraction of the actual equiaxed grains can be obtained from the Avrami equation:

$$\emptyset = 1 - \exp[-\emptyset_e] \quad (16)$$

where \emptyset is the volume fraction of actual equiaxed dendrites and \emptyset_e is the extended volume fraction. It can be assumed that the dendrites grow spherically.

$$\emptyset_e = \frac{4\pi r_e^3 N_0}{3} \quad (17)$$

Here, N_0 is the number of heterogeneous nucleation sites per unit volume. According to the Hunt criterion [33], the critical transition temperature gradient and solidification rate of the CET can be obtained using the volume fraction of equiaxed dendrites at the growth interface of columnar dendrites under different growth conditions.

Figure 10 shows the CET curve of Inconel 625; in the area above the red line, the volume fraction of equiaxed dendrites exceeds 49%, and this area corresponds to the fully equiaxed dendrites zone. Below the black line, the volume fraction of equiaxed dendrites is less than 0.66%, and this area contains fully columnar dendrites. The blue squares represent the solidification conditions (G, V) for Inconel 625 during the LSF process. Labels A–F correspond to the positions of the 1st layer, 2nd layer, 4th layer, 8th layer, 16th layer, and 25th layer, respectively. It can be seen that the solidification condition at the bottom of the molten pool for all the deposited layers satisfies the growth conditions of columnar dendrites, whereas that at the top of the molten pool satisfies the growth conditions of equiaxed dendrites. In addition, as the deposition height increases, the solidification conditions become more conducive for the formation of equiaxed dendrites. As a result, the equiaxed dendrites appear in the top region of each layer. Because the top region of each layer can be re-melted by the next deposition cycle, the previous equiaxed dendrites will disappear and the top zone of the deposit will retain only some equiaxed dendrites.

Dynamic recrystallisation

Figure 11 shows the distribution of recrystallised grains in different zones of the deposit, as obtained using the recrystallisation module of EBSD. The blue

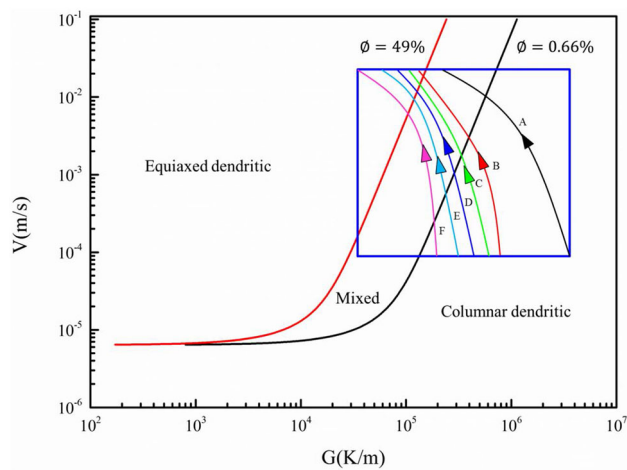


Figure 10 Microstructure selection map for Inconel 625 superalloy under the experiment conditions described in the article, showing the expected solidification morphology as a function of temperature gradient, G , and solidification velocity, V . $\Delta T_n = 2.5K$, $N_0 = 10^{12}/m^3$.

area represents the recrystallisation region, whereas the red areas represent the deformation region. The recrystallisation volume fractions in the bottom and top zones of the deposit were close to 56%; however, the middle zone was recrystallised to a greater extent, with the recrystallisation volume fraction being about 80%. Additionally, the size of recrystallised grains was smaller; these grains were distributed mainly along the grain boundaries, and some small recrystallised grains were formed inside the large grains.

Figure 12 shows the orientation imaging microscopy (OIM) maps of the bottom zone of the deposit; here, microstructural characteristics corresponding to discontinuous DRX (DDRX) and continuous DRX (CDRX) processes can be observed. In the OIM maps, the high-angle grain boundaries (HAGBs) and low-angle grain boundaries (LAGBs) are represented by black lines and blue lines, respectively. HAGBs refer to grain boundaries with misorientation angles larger than 15° , and LAGBs refer to grain boundaries with misorientation angles in the range of 2° – 5° . Grain boundaries with misorientation angles in the range of 5° – 15° are known as medium-angle grain boundaries (MAGBs), and they are represented by green lines in the present OIM maps.

The yield strength of the Inconel 625 superalloy decreases significantly with increasing temperature. Therefore, the resulting high thermal stress leads to plastic deformation of the deposit during the LSF process. Additionally, the temperature of the deposit is extremely high owing to the subsequent thermal cycling and heat accumulation. In FCC metals, which have low SFEs, DRX can occur during the LSF process. Depending on the mechanism of DRX, it is classified as discontinuous DRX (DDRX) or continuous DRX (CDRX). In Fig. 12a, it can be seen that many small dynamically recrystallised grains are formed around the original grain boundaries, and these newly formed grains are composed of HAGBs. This grain boundary morphology indicates that the nucleation mechanism is DDRX, which is caused by strain-induced grain boundary migration. Figure 14a shows the bright-field TEM images of recrystallised grains newly formed along the grain boundaries. It is found that no dislocations are present in the newly formed grains. In the DDRX process, the recrystallised grains mainly nucleate and grow at the original grain boundaries and trigeminal grain boundaries. The typical microstructure characteristics for the DDRX are that the original grain boundaries

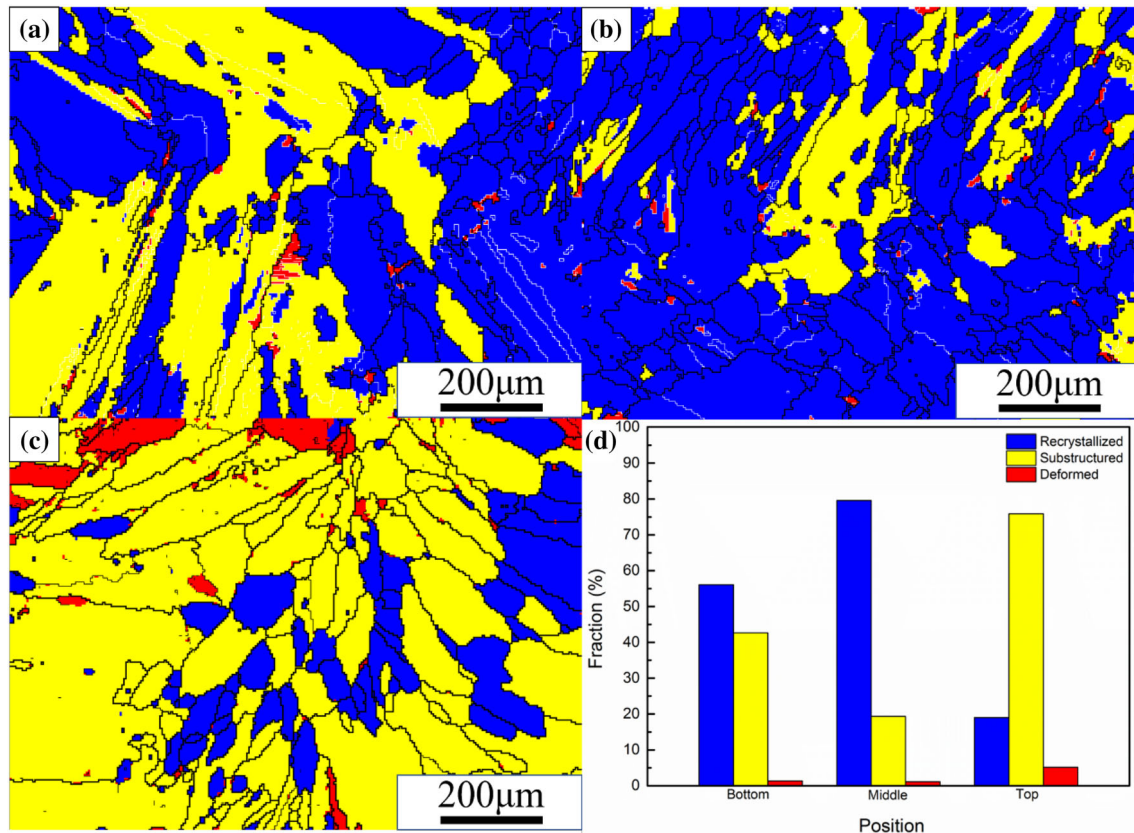


Figure 11 Recrystallisation grain distribution and recrystallisation volume fraction of different zones. **a** The bottom zone; **b** the middle zone; **c** the top zone; and **d** fraction of recrystallisation grains.

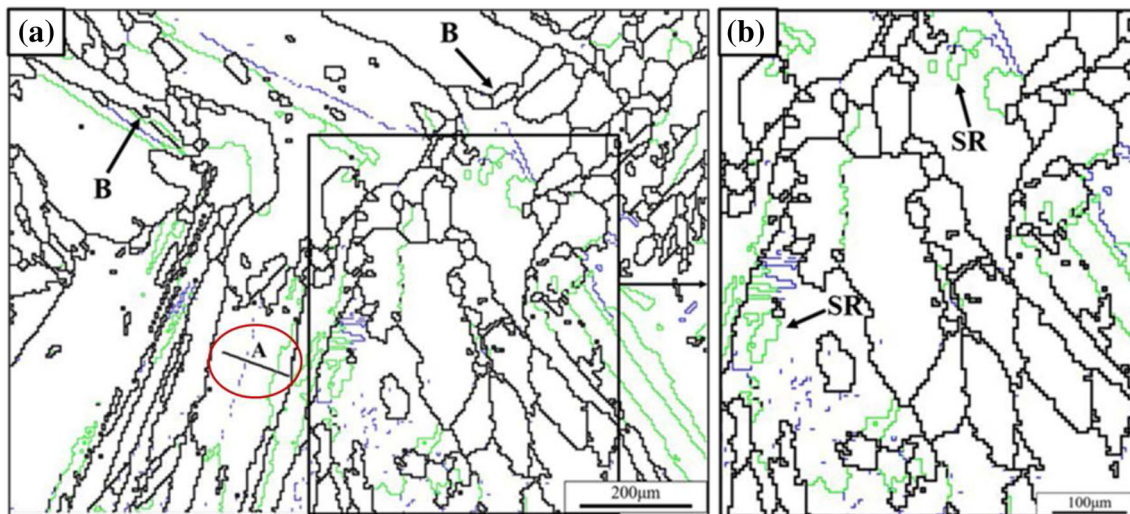


Figure 12 a Microstructural evolution of the bottom zone in deposition. Arrows represent recrystallised grains by DDRX. **b** Detailed view of the CDRX mechanism by progressive rotation of LAGBs. OIM maps boundary distribution for HAGBs ($> 15^\circ$),

black lines, and LAGBs ($2\text{--}5^\circ$), blue lines, and MAGBs ($5\text{--}15^\circ$), green lines. SR: sub-grain rotation and B: bulging of grain boundaries.

become bulging and present jagged, which are indicated by the arrow labelled 'B' in Fig. 12a.

However, microstructural features evidencing the occurrence of CDRX can also be observed in Fig. 12b:

some small recrystallised grains and MAGBs are formed inside the original grains. Some low-angle sub-grain boundaries are formed inside the original grains, and as the deformation progresses, these sub-grain boundaries (SGBs) rotate by constantly absorbing dislocations and become HAGBs. As a result, fine recrystallised grains are formed inside the original grains, and sub-grains with a high density of LAGBs form HAGBs owing to an increase in the misorientation. Li et al. [15] revealed that the mechanism of CDRX is progressive sub-grain rotation until a misorientation angle between 10° and 15° is attained. Figure 13 shows the results of misorientation analysis along line A in Fig. 12a; it can be seen that most of the point-to-point misorientations are smaller than 2° ; however, the cumulative misorientations from the original point exceed 10° . This indicates accumulation of the misorientation between a grain and a grain boundary, which results in an increase in the misorientation gradient; as a consequence, the SGB can rotate to form HAGBs. Additionally, it can be seen from Fig. 14b that the deformation causes piling up of the dislocations and their rearrangement to form a dislocation wall and SGBs during the CDRX process.

Textures of metal polycrystals are usually confirmed by the $\{hkl\}$ crystallographic plane and $\langle uvw \rangle$ direction. Figure 15 shows the crystallographic data obtained from the EBSD maps (Fig. 15a), which are transformed to orientation

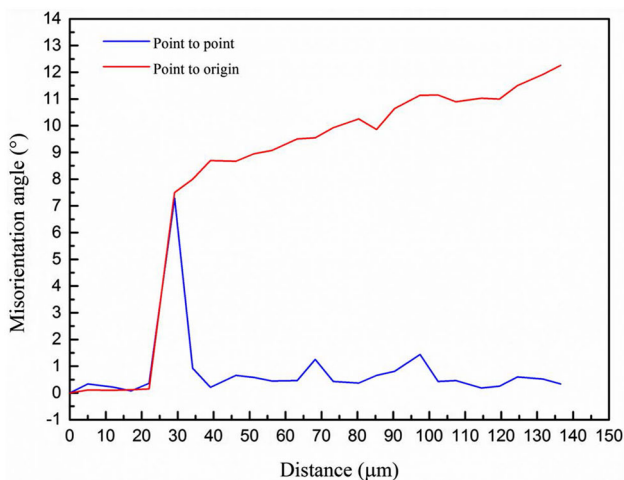


Figure 13 Misorientations analysis along line A marked in Fig. 4a, the red line shows the misorientation between each point to the first point, and the blue line indicates the misorientation between point to point along line A.

distribution functions (ODFs) of $\varphi_1 = 0^\circ$ and $\varphi_1 = 45^\circ$ sections (Fig. 15b) in the middle zone of the deposit. It is found that the deposit has a strong rotated cube (R) texture [cube, rotated by 45° around the normal direction (ND)], with a $\{001\} \langle 110 \rangle$ component. The R texture often appears during the recrystallisation of FCC metals; it is a typical recrystallisation texture and is observed during the friction stir welding (FSW) of the Inconel 625 superalloy [34]. During the deformation of metal materials, the dislocations slip along the plane and direction with the densest atomic packing. A total of 12 slip systems are present in FCC metal materials, which are obtained by the combination of a slip plane and a slip direction, that is, 4 independent $\{111\}$ slip planes and 3 unique $\langle 110 \rangle$ directions in each plane [35]. Therefore, the rotation and slip of grains occur mainly in the $\langle 110 \rangle$ direction, and the R texture appears mostly during the deformation and recrystallisation processes.

DDRX and CDRX in the Inconel 625 superalloy have been observed and confirmed during thermo-mechanical processes such as FSW and high-temperature deformation [34, 36]. Guo et al. [36] investigated the microstructural models of DRX in hot-deformed Inconel 625, and they found that the deformation temperature and strain rate were the main factors influencing DRX. In addition, an increase in the deformation temperature or decrease in the strain rate led to earlier initiation of DRX, and the nucleation mechanisms of DRX in the alloy included DDRX and CDRX. Though the strains in FSW and high-temperature deformation are higher than the thermal strain in LSF, the true strain in high-temperature deformation can reach 50% or even higher; however, the thermal strain in LSF cannot exceed 5% [37]. Nevertheless, the FEM results of the temperature field in the deposit during the LSF process (Fig. 6) show that the temperatures of most of the deposited layers are mainly in the range of $800\text{--}1050^\circ\text{C}$, and the temperature in deposit is much higher than that in the FSW process. Figure 16 shows the thermal stress evolution along the length direction in the centre plane of the deposit during the LSF process. It can be found that the thermal stress can exceed 600 MPa whether tensile stress or compressive stress during the LSF process, it is much higher than the yield stress of Inconel 625. Therefore, the plastic deformation will take place during the LSF process. On the other hand, owing to the repeated

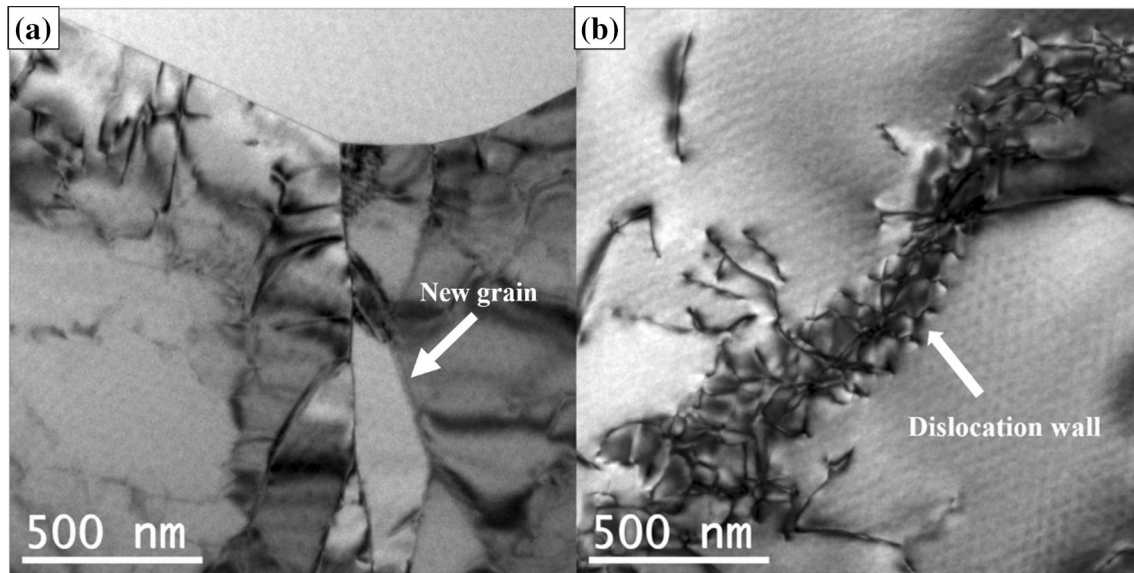


Figure 14 Bright filed TEM images of the recrystallisation mechanism in the deposition sample of Inconel 625. **a** New recrystallised grains in the grain boundary. **b** Rearrangement of the dislocations during the CDRX.

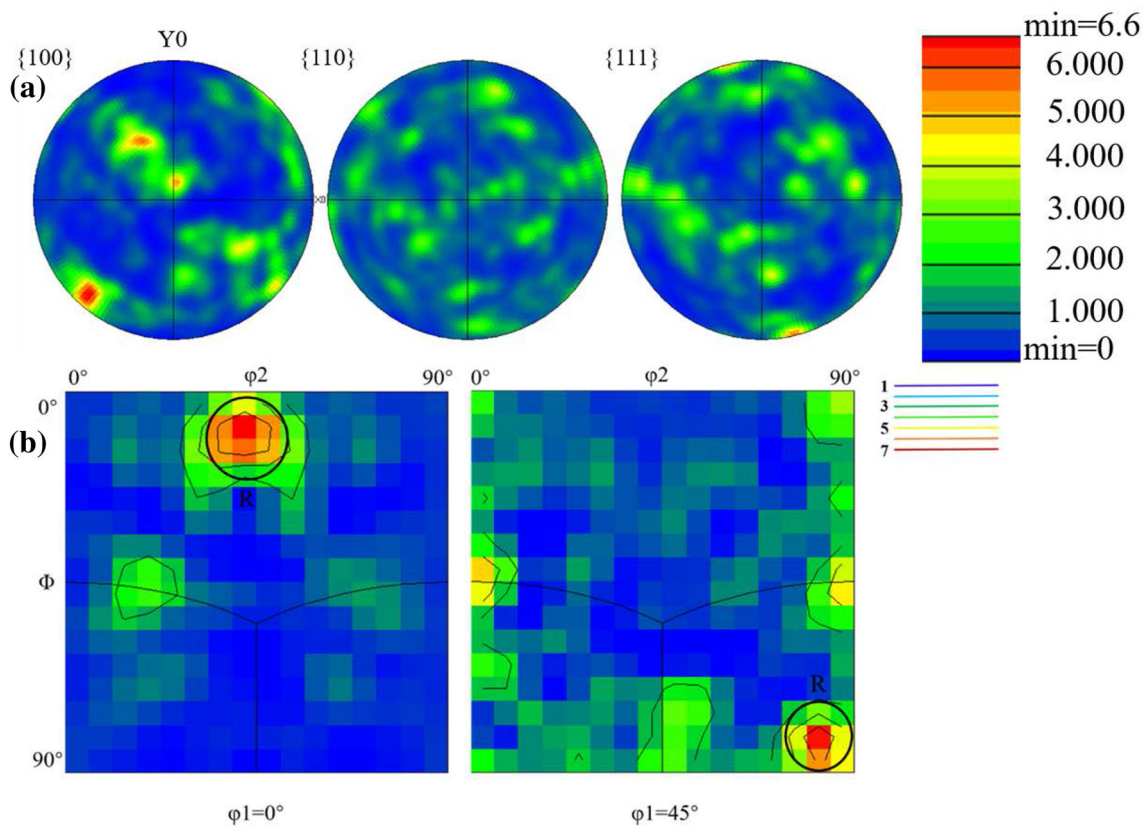
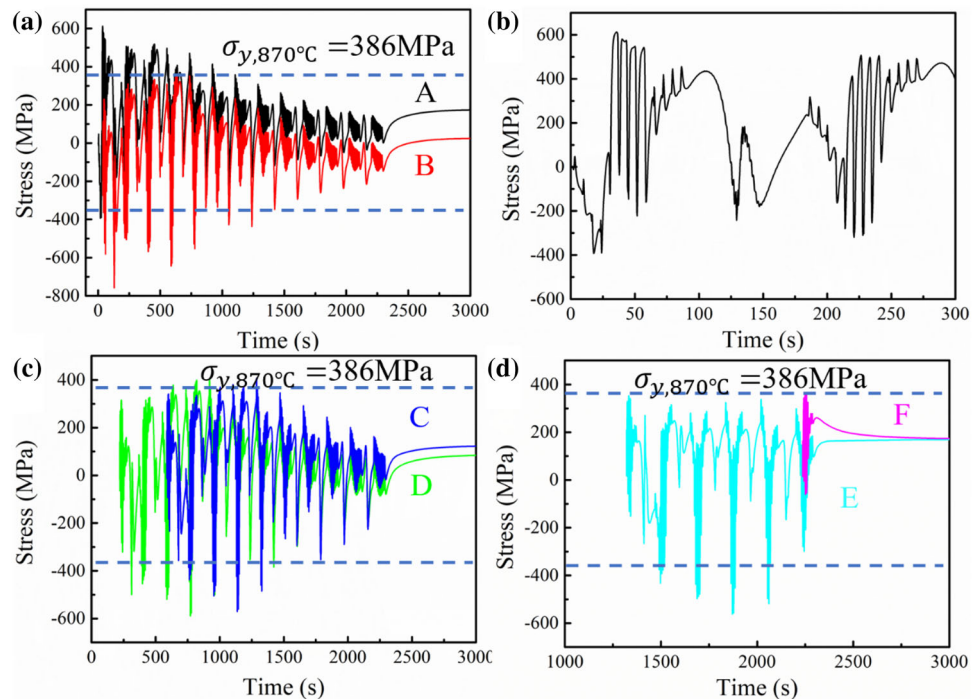


Figure 15 **a** Pole figure of the middle zone in deposit; **b** ODF figure at $\phi_1 = 0^\circ$ and $\phi_1 = 45^\circ$.

thermal cycling and high cooling rate during the LSF process, the strain rate is very high; this high strain rate promotes the nucleation of DRX. Jiang et al. [38]

investigated the effects of strain rate on the DRX mechanism of alloy 617B and found that the DRX process is controlled mainly by the growth of DRX

Figure 16 The thermal stress along the length direction in the centre plane of the built as a function of time simulated by FEM. **a** Thermal stress evolution of points A and B; **b** detailed thermal stress evolution of point A; **c** thermal stress evolution of points C and D; **d** thermal stress evolution of points E and F.



nuclei under the low-strain-rate condition and that the DRX nucleation rate is high at high strain rates. A high strain rate can induce the generation of adiabatic heat, which can enhance the DRX nucleation to promote the occurrence of DRX [39]. Furthermore, a larger amount of energy is stored under the high-strain-rate condition, which can decrease the critical radius of dynamically recrystallised nuclei; this, in turn, would facilitate DRX nucleation. In addition, the migration of grain boundaries is promoted when the amount of stored energy is large [40]. Furthermore, a higher strain rate leads to an increased dislocation density, which can cause a reduction in the recrystallisation temperature. As a result, the high strain rate and high temperature range in the deposit promote the nucleation and growth of DRX, and DRX occurs during the LSF process.

Ma et al. [41] investigated the crystallographic texture of Inconel 625 fabricated by LSF. They found that the $\langle 100 \rangle$ -direction of most grains was aligned with the scanning direction, where the $\langle 100 \rangle$ -direction included a strong Goss texture component ($\{011\} \langle 100 \rangle$) and a relatively weaker cubic texture ($\{001\} \langle 100 \rangle$). However, a recrystallisation texture and recrystallised grains were not observed in their sample. This is mainly because in their LSF process, the deposited sample was small and its width was only 7 mm; consequently, accumulation of heat was

difficult, the temperature of the deposited layers was not too high, and the deposition time was short, and because of all these factors, the critical conditions for DRX could not be achieved. Therefore, only a solidification texture was observed in the $\langle 100 \rangle$ -direction in the deposited Inconel 625 superalloy.

Recently, EBSD technology has been widely used to characterise the local plastic strain in different metals during deformation [42, 43]. Figure 17a–c shows the local strain distributions in the different zones of the deposit, and Fig. 16d shows the distribution of the misorientation angle relative to the central orientation in the different zones. Comparison of the distributions in Fig. 17 with the distribution of recrystallised grains in Fig. 11 reveals that the region of higher local strain corresponds to the region where recrystallisation did not occur. It can be seen that the local strain in the middle zone of the deposit is smaller than those in the top and bottom zones. However, the misorientation angle distribution shows that the misorientation of the middle zone is also smaller. Because the driving force for DRX is stored deformation energy, after DRX occurs, dislocations are released and there is no distortion in the recrystallised grains. The number and density of stored dislocations increase with increasing extent of plastic deformation, and this leads to an increase in the range of crystal orientations within a grain. As a

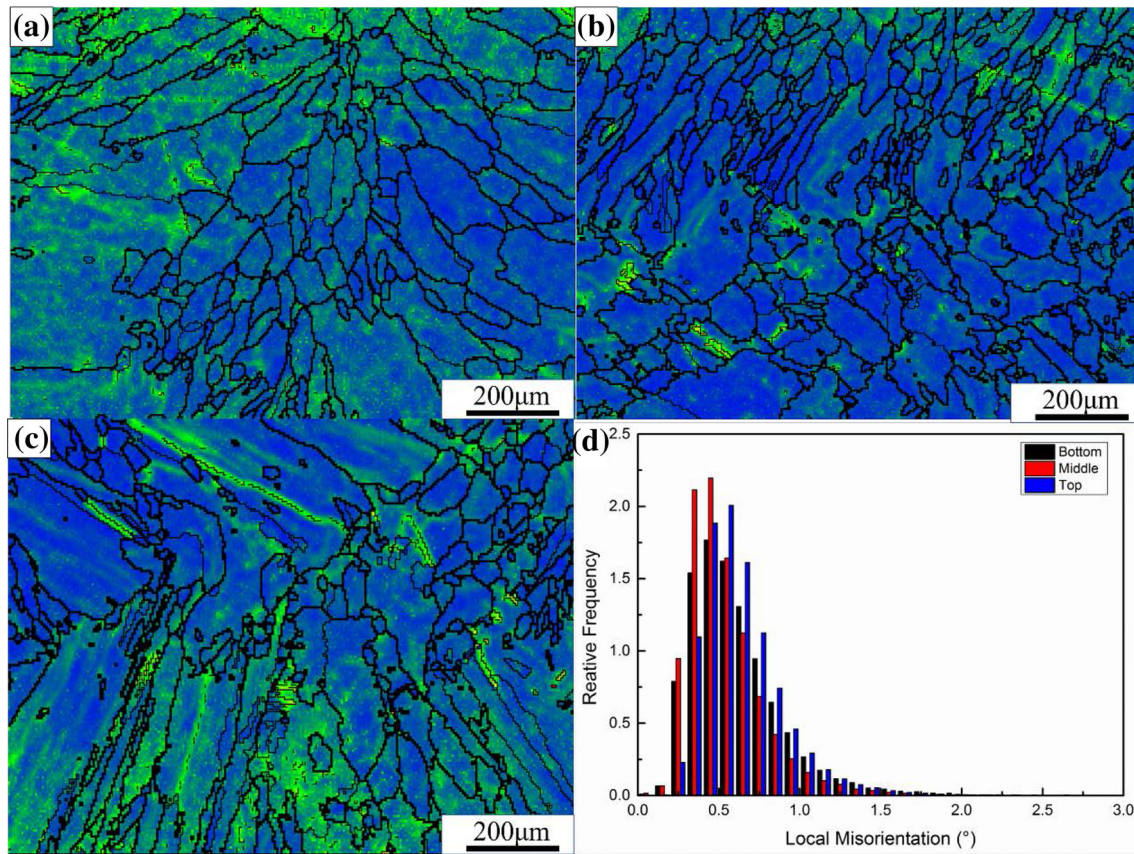


Figure 17 EBSD-analysed strain component images of different zones: **a** top zone, **b** middle zone, **c** bottom zone. And **d** distribution of misorientation angle from central orientation in different zones.

result, the recrystallised grains are smaller than the original grains and the local strain is lower after DRX occurs.

DDRX and CDRX are observed to occur in the Inconel 625 superalloy during thermomechanical processes such as FSW and high-temperature deformation. From the analyses in previous works, it is found that DRX can occur during the LSF process. This finding establishes the basis for a new method for controlling the microstructure in the LSF process and is useful in understanding the microstructural evolution during the LSF process.

Conclusions

The present study investigated the microstructural evolution during the LSF process, including the solidification and DRX processes occurring during LSF. The following conclusions can be drawn from the findings of the study.

- (1) The grain sizes and morphologies in different zones of the deposited sample are different; the columnar grains in the bottom zone are smaller than those in the middle zone owing to the epitaxial growth of substrate grains. The top zone undergoes the CET to form equiaxed grains. The columnar and equiaxed grains have a periodic microstructure.
- (2) Because the solidification rate decreases as the deposition height increases, the primary dendrite arm spacing (λ_1) gradually increases from the bottom zone to the top zone. Meanwhile, the secondary dendrite arm gradually becomes more apparent. Although the microsegregation of the Nb element in the top zone is weaker, the Laves phase has a longer growth time and a larger growth space than bottom region. As a result, the Laves phase becomes larger with increasing height of the deposit.
- (3) DRX, including CDRX and DDRX, occurs in all the zones during the LSF process, and the recrystallised grains are distributed mainly in

the grain boundaries. An R texture (cube, rotated by 45° around the ND) with a {001} <110> component is observed in the deposit; this texture often appears during deformation and recrystallisation processes. Because the driving force for DRX is the stored deformation energy, after DRX occurs, dislocations are released and there is no distortion in the recrystallised grains.

Acknowledgements

The work was supported by National Natural Science Foundation of China (Nos. 51604227, 51501154 and 51565041), National Key Research and Development Plan of China (No. 2016YFB1100104), the Fundamental Research Funds for the Central Universities of China (Nos. 3102015BJ(II)ZS013 and 3102017jg02013), and the Natural Science Foundation of Shaanxi Province of China (2017JM5052).

References

- [1] Shoemaker LE (2005) In: Loria EA (ed) Superalloys 718, 625, 706 and various derivatives. TMS, Warrendale, pp 409–418
- [2] Valencia JJ, Spirko J, Schmees R (1997) In: Loria EA (ed) Superalloys 718, 625, 706 and various derivatives. TMS, Warrendale, pp 753–762
- [3] Chaudhuri A et al (2017) Microstructural evolution of cold-sprayed Inconel 625 superalloy coatings on low alloy steel substrate. *Acta Mater* 129:11–25
- [4] Carroll BE et al (2016) Functionally graded material of 304L stainless steel and inconel 625 fabricated by directed energy deposition: characterization and thermodynamic modeling. *Acta Mater* 108:46–54
- [5] Mostafaei A et al (2017) Microstructural evolution and mechanical properties of differently heat-treated binder jet printed samples from gas- and water-atomized alloy 625 powders. *Acta Mater* 124:280–289
- [6] English CL, Tewari SK, Abbott DH (2011) An overview of Ni base additive fabrication technologies for aerospace applications. pp 397–412
- [7] Wang Z et al (2017) Residual stress mapping in Inconel 625 fabricated through additive manufacturing: method for neutron diffraction measurements to validate thermomechanical model predictions. *Mater Des* 113:169–177
- [8] Bussu G, Irving PE (2003) The role of residual stress and heat affected zone properties on fatigue crack propagation in friction stir welded 2024-T351 aluminium joints. *Int J Fatigue* 25(1):77–88
- [9] Moat RJ et al (2011) Residual stresses in laser direct metal deposited Waspaloy. *Mater Sci Eng, A* 528(6):2288–2298
- [10] Hu YL et al (2016) Effect of heat input on cracking in laser solid formed DZ4125 superalloy. *Opt Laser Technol* 86:1–7
- [11] Hu YL et al (2017) Effect of Ti addition on cracking and microhardness of Inconel 625 during the laser solid forming processing. *J Alloy Compound* 711:267–277
- [12] Denlinger Erik R, Pan M (2016) Effect of stress relaxation on distortion in additive manufacturing process modeling. *Addit Manuf* 12:51–59
- [13] Mukherjee T et al (2017) Mitigation of thermal distortion during additive manufacturing. *Scripta Mater* 127:79–83
- [14] Mukherjee T, Zhang W, Debroy T (2017) An improved prediction of residual stresses and distortion in additive manufacturing. *Comput Mater Sci* 126:360–372
- [15] Li D et al (2011) The microstructure evolution and nucleation mechanisms of dynamic recrystallization in hot-deformed Inconel 625 superalloy. *Mater Des* 32(2):696–705
- [16] Humphreys FJ, Hatherly M (2004) Recrystallization and related annealing phenomena, 2nd edn. Elsevier, Amsterdam
- [17] Dinda GP, Dasgupta AK, Mazumder J (2009) Laser aided direct metal deposition of Inconel 625 superalloy: microstructural evolution and thermal stability. *Mater Sci Eng A* 509(1–2):98–104
- [18] Liu F et al (2014) Evolution of interface and crystal orientation of laser solid formed GH4169 superalloy during recrystallization. *Acta Metall Sin* 50(4):463–470
- [19] Chiumenti M et al (2017) Numerical simulation and experimental calibration of additive manufacturing by blown powder technology. Part I: thermal analysis. *Rapid Prototyp J* 23(2):448–463
- [20] INCONEL alloy 625, Spec. Met. Corp. <http://www.specialmetals.com/documents/Inconelalloy625.pdf>2013
- [21] Denlinger Erik R, Pan M (2016) Effect of stress relaxation on distortion in additive manufacturing process modeling. *Addit Manuf* 12:51–59
- [22] Kurz W, Fisher DJ (1992) Fundamentals of Solidification, 3rd edn. Aedermansdorf, Trans Tech Publications, Switzerland
- [23] Dupont J, Robino NCV, Marder AR (1998) Modeling solute redistribution and microstructural development in fusion welds of Nb-bearing superalloys. *Acta Mater* 46(13):4781–4790
- [24] Dupont JN et al (1998) Solidification of Nb-bearing superalloys: part II. Pseudoternary solidification surfaces. *Metall Mater Trans A* 29(11):2785–2796

- [25] Manvatkar V, De A, Debroy T (2014) Heat transfer and material flow during laser assisted multi-layer additive manufacturing. *J Appl Phys* 116(12):133
- [26] An Ke et al (2017) Neutron residual stress measurement and numerical modeling in a curved thin-walled structure by laser powder bed fusion additive manufacturing. *Mater Des* 135:122–132
- [27] Hu D, Kovacevic R (2003) Modelling and measuring the thermal behaviour of the molten pool in closed-loop controlled laser-based additive manufacturing. *Proc Instit Mech Eng Part B J Eng Manuf* 217(4):441–452
- [28] Mokadem S et al (2007) Laser repair of superalloy single crystals with varying substrate orientations. *Metall Mater Trans A* 38(7):1500–1510
- [29] Kurz W, Bezençon C, Gäumann M (2016) Columnar to equiaxed transition in solidification processing. *Sci Technol Adv Mater* 2(1):185–191
- [30] Gäumann M et al (2001) Single-crystal laser deposition of superalloys: processing–microstructure maps. *Acta Mater* 49(6):1051–1062
- [31] Ren YM et al (2017) Microstructure and deformation behavior of Ti-6Al-4 V alloy by high-power laser solid forming. *Acta Mater* 132:82–95
- [32] Lin X et al (2003) Columnar to equiaxed transition during alloy solidification. *Sci China (Ser E)* 46(5):475–489
- [33] Hunt JD (1984) Steady state columnar and equiaxed growth of dendrites and eutectic. *Mater Sci Eng* 65:75–83
- [34] Fernandez Johnnatan Rodriguez, Ramirez AJ (2017) Microstructural Evolution During Friction Stir Welding of Mild Steel and Ni-Based Alloy 625. *Metall Mater Trans A* 48:1–11
- [35] Dieter GE (1988) *Mechanical Metallurgy*. McGraw-Hill, New York
- [36] Guo QM, Li DF, Guo SL (2012) Microstructural Models of Dynamic Recrystallization in Hot-Deformed Inconel 625 Superalloy. *Adv Manuf Process* 27(9):990–995
- [37] Zhao HY et al (2009) Temperature and stress fields of multi-track laser cladding 19(s2):s495–s501
- [38] Jiang H et al (2016) A study on the effect of strain rate on the dynamic recrystallization mechanism of alloy 617B. *Metall Mater Trans A* 47(10):5071–5087
- [39] Wang J et al (2013) Hot working characteristics of nickel-base superalloy 740H during compression. *Mater Sci Eng Struct Mater Prop Microstruct Process* 566(2):61–70
- [40] Sun HQ et al (2007) Plastic strain-induced grain refinement in the nanometer scale in a Mg alloy. *Acta Mater* 55(3):975–982
- [41] Ma D et al (2017) Crystallographic texture in an additively manufactured nickel-base superalloy. *Mater Sci Eng, A* 684:47–53
- [42] Kamaya M (2011) Assessment of local deformation using EBSD: quantification of accuracy of measurement and definition of local gradient. *Ultramicroscopy* 111(8):1189
- [43] Kamaya M, Wilkinson AJ, Titchmarsh JM (2006) Quantification of plastic strain of stainless steel and nickel alloy by electron backscatter diffraction. *Acta Mater* 54(2):539–548